Weakly nonlinear analysis of the Saffman-Taylor problem in a radially spreading fluid annulus

Pedro H. A. Anjos* and Shuwang Li†
Department of Applied Mathematics, Illinois Institute of Technology, Chicago, Illinois 60616, USA

(Received 10 October 2019; accepted 15 April 2020; published 8 May 2020)

We study viscous fingering formation in an immiscible three-layer radial Hele-Shaw flow, where two coupled interfaces spread radially. More specifically, we examine how the initial distance d between the inner and outer interfaces (i.e., annulus' thickness) influences the shape of the emerging fingering patterns. Our theoretical analysis extends the perturbation theory beyond linear stability to a second-order mode-coupling theory. An important feature of our second-order perturbative approach is the fact that through the coupling of the appropriate Fourier modes, one is able to extract key analytical information about the morphology of the interface at the onset of nonlinearities. Under the circumstances where the inner interface is unstable and the outer one is stable, our theoretical results indicate that as d decreases, the coupling between the interfaces becomes stronger and the nearly matched final shapes exhibit the formation of wide fingers with bifurcated tips. However, if d is reduced further, we observe an unexpected change in the morphology of the patterns, where the conventional finger-splitting morphologies are replaced by polygonal-like structures with narrow fingers. The opposite scenario where the inner interface is stable and the outer one is unstable reveals two interesting situations: the onset of formation of drops due to the rupture of the intermediate layer of fluid, and an overall stabilization of the outer interface by the presence of the fluid annulus.

DOI: 10.1103/PhysRevFluids.5.054002

I. INTRODUCTION

The Saffman-Taylor problem [1], or viscous fingering phenomenon, addresses the hydrodynamic instability that arises when a fluid displaces another fluid of higher viscosity in a porous medium or in a confined geometry of a Hele-Shaw cell [2]. In the effectively two-dimensional (2D) setup of a Hele-Shaw cell, the lower viscosity fluid penetrates the more viscous one and the fluid-fluid interface becomes unstable. The dynamic competition between surface tension and viscous forces (or pressure gradients) leads to the development of finger-like structures. One popular and widely investigated version of the Saffman-Taylor problem is the radial Hele-Shaw flow driven by injection [3–15], where the less viscous fluid is injected into the more viscous one through a small inlet located at the center of the upper glass plate. In such injection-driven flow, as the interface expands, finger-like structures form, spread outward, compete among themselves and split at their tips, originating multiply ramified interfacial patterns. In this scenario, one can say that finger-tip splitting and finger competition are basic nonlinear mechanisms of the viscous fingering process. It is worthwhile to mention that, in the framework of the classic Saffman-Taylor problem, there is no instability when a more viscous fluid displaces a less viscous one. In this situation, the two-fluid boundary grows as a circular interface in radial Hele-Shaw cells.

*pamorimanjos@iit.edu
†sli15@iit.edu

Over the past several decades this two-fluid radial displacement has been actively investigated. Despite the large number of numerical [12–15] and experimental [5–11] studies already performed, most work in the literature has focused on the motion of only two layers of fluids separated by one interface. However, in some practical applications such as chemical-enhanced oil recovery, a sequence of different layers of fluids are used in succession to displace a resident fluid in a porous medium. Depending on the number of injected fluid layers, there can be more than one interface involved in this process. With an appropriate choice of the properties of the injected fluids and the correct injection policy, the viscous fingering formation can be drastically reduced and thus maximize the productivity of oil reservoirs. Therefore, in order to improve the usefulness of such important oil recovery strategy, it is necessary to understand the pattern-forming dynamics that arises from this intricate multilayer displacement.

Interestingly, the study of the Saffman-Taylor problem in multilayer radial Hele-Shaw flows has been considerably unappreciated compared to those equivalent studies that investigate the motion of only two fluids [3–15]. Actually, very few groups have performed studies on flows with more than two fluid layers. Some time ago, Cardoso and Woods [16] carried out theoretical and experimental investigations of an immiscible three-layer radial displacement. In such a two-interface system, an intermediate layer of fluid (also known as intermediate annulus) is bounded by two other fluids of different viscosities. Linear stability analysis of the thin intermediate layer showed that there is a global mode which is determined only by the viscosities of the bounding fluids and an internal mode that dictates the local stability of the two interfaces [16]. By choosing a highly viscous inner fluid, they focused on the case in which the inner interface is stable and the outer one is unstable. They verified experimentally that, due to the growth of disturbances on the outer interface, the thin annular region breaks up into drops when the interfaces meet during radial injection process in Hele-Shaw cell. More recently, Beeson-Jones and Woods [17] revisited the dual-interface problem but now focusing on the case where both interfaces are unstable, and found the optimal value of the viscosity of the intermediate fluid in order to inject fluid at the fastest rate possible while maintaining a stable flow.

Daripa and collaborators have also contributed to the development of studies related to multilayer flows in both rectangular [18–20] and radial [21] Hele-Shaw cell geometries. In Ref. [21], for instance, the authors considered a multilayer radial Hele-Shaw flow and performed a linear stability analysis of an arbitrary number of fluid layers to obtain dispersion relations and upper bounds on the growth rate. Then they used these findings to design more stable injection schemes.

In all these aforementioned studies [16–21], it should be emphasized that the only analytical tool utilized was linear stability analysis. Therefore, except for the advance-time experiments carried out in Ref. [16], all the analytical investigations performed in Refs. [16–21] are restricted to the early-time, purely linear regime in injection-driven three-layer radial Hele-Shaw flows. Although this analytical tool provides a good understanding of the pattern-formation process in the initial time regime and gives insights into possible control mechanisms of viscous fingering formation, it cannot assess the effects of the intermediate fluid annulus on the system's nonlinear pattern-forming dynamics. Therefore, a systematic study of the influence of the intermediate fluid annulus on the most salient morphological features of the patterns arising in injection-driven three-layer radial Hele-Shaw flows is still lacking.

Our main purpose in this work is to extend the perturbation theory beyond linear stability (i.e., to a second-order mode-coupling theory) and carry out a weakly nonlinear analysis for the intermediate stages of the coupled dual-interface evolution in a three-layer radial Hele-Shaw flow, focusing on the onset of nonlinear effects. More specifically, we aim to examine the influence of the initial distance between the inner and outer interfaces (i.e., annulus' thickness) on the shape of the emerging fingering patterns, mainly on its impact on finger-tip broadening, splitting, and narrowing events, as well as on finger competition dynamics, for both interfaces. Our analytical second-order mode-coupling theory permits access to the onset of intrinsically nonlinear pattern-forming mechanisms, just by considering the interplay between a small number of perturbative Fourier modes. In addition, our weakly nonlinear equations are valid to arbitrary values of viscosity ratios, and thus the analysis is performed considering two different cases of interest: in the first case, fluid viscosities are chosen

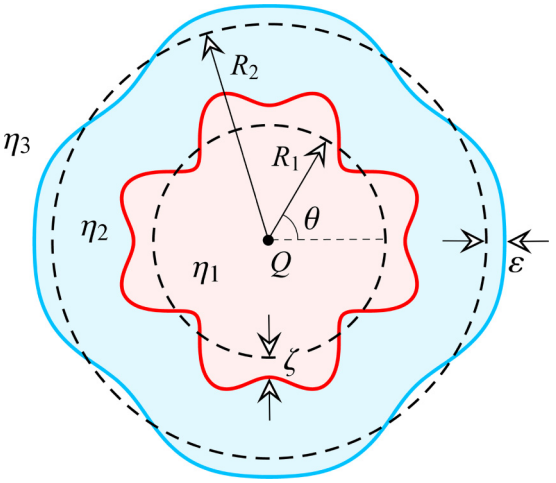

FIG. 1. Schematic illustration (top view) of the injection-driven three-fluid motion in a radial Hele-Shaw cell geometry. The outermost fluid 3 and the innermost fluid 1 are separated by an annulus of fluid 2. The trailing interface is represented by the solid red line, and the leading interface is depicted by the solid blue line. The inner and outer dashed curves represent the time-dependent unperturbed radii of the trailing (R_1) and leading (R_2) interfaces, respectively. Fluid 1 is injected at a constant injection rate Q through an inlet (illustrated by a small dot) located at the center of the upper plate.

as such that the inner interface is unstable while the outer is stable. Then we consider the opposite case where the inner interface is stable and the outer one is unstable due to a positive viscosity jump. Note that the motivation for this study is not restricted to the enhancement of oil recovery strategies. In addition to its intrinsic scientific and academic value, the study has applications for many fields, including cell fragmentation, growth of tumors, mixing in multiphase flow, crystal growth, and flow in granular media.

The remainder of this paper is structured as follows. In Sec. II we present a derivation of a set of coupled weakly nonlinear equations that describe the time evolution of the interfacial perturbation amplitudes for both the inner and outer interfaces under injection-driven radial Hele-Shaw flow circumstances. In Sec. III we focus on discussing the role played by the annulus' thickness in regulating the overall shape of the fingers and also the finger competition behavior, considering two distinct cases for the stability of the interfaces (Secs. III A and III B). Finally, in Sec. IV we summarize our main results and provide some concluding remarks.

II. MODE-COUPLING DIFFERENTIAL EQUATIONS FOR THE PERTURBATION AMPLITUDES

Consider a Hele-Shaw cell of constant gap b containing three layers of immiscible, incompressible, Newtonian fluids and denote the viscosities of the fluids as η_1, η_2, and η_3, as depicted in Fig. 1. Here an intermediate layer of fluid 2 separates the innermost fluid 1 from the outermost fluid 3. Between fluids 1 and 2 (2 and 3) there exists a surface tension σ_{12} (σ_{23}). The inner fluid is injected at a constant injection rate Q (equal to the area covered per unit time) through an inlet located at the center of the upper plate. In contrast to the conventional two-fluid system [3–15], here we have two interfaces: the first one is located between fluids 1 and 2, and is commonly referred to as trailing interface, while the second one, also known as leading interface, is positioned between fluids 2 and 3.

During the injection process, the initially slightly perturbed, circular interfaces can become unstable, and deform, due to the interplay of viscous and capillary forces. Therefore, we express the perturbed trailing interface as $\mathcal{R}_1 = \mathcal{R}_1(\theta, t) = R_1(t) + \zeta(\theta, t)$, where $R_1 = R_1(t) = \sqrt{R_1^2(0) + Qt/\pi}$ is the time-dependent unperturbed radius of the trailing interface, and θ denotes

the azimuthal angle in the $r-\theta$ plane. The radial coordinate r denotes the distance to the injection source point, which is chosen as the origin of the polar coordinate system. The net interface disturbance is represented as a Fourier series

$$\zeta(\theta,t)=\sum_{n=-\infty}^{+\infty}\zeta_n(t)\,e^{in\theta}, \tag{1}$$

where $\zeta_n(t)$ denotes the complex Fourier amplitudes, with integer wave numbers n. Likewise, we represent the perturbed leading interface as $\mathcal{R}_2=\mathcal{R}_2(\theta,t)=R_2(t)+\varepsilon(\theta,t)$, where $R_2=R_2(t)=\sqrt{R_2^2(0)+Qt/\pi}$ and

$$\varepsilon(\theta,t)=\sum_{n=-\infty}^{+\infty}\varepsilon_n(t)\,e^{in\theta}. \tag{2}$$

Our perturbative approach keeps terms up to the second order in ζ and ε. In both Fourier expansions of ζ and ε we include the $n=0$ mode to maintain the area of the perturbed shapes independent of the perturbations. Mass conservation imposes that the zeroth mode is written in terms of the other modes as $\zeta_0=-\frac{1}{2R_1}\sum_{n=1}^{\infty}[|\zeta_n(t)|^2+|\zeta_{-n}(t)|^2]$. Similarly, we have $\varepsilon_0=-\frac{1}{2R_2}\sum_{n=1}^{\infty}[|\varepsilon_n(t)|^2+|\varepsilon_{-n}(t)|^2]$. Note that the trailing and leading interfaces move radially outward with velocities $\dot{R}_1=Q/(2\pi R_1)$ and $\dot{R}_2=Q/(2\pi R_2)$, respectively. Therefore, during the flow there is a continuous thinning of the fluid annulus since $\dot{R}_1>\dot{R}_2$.

The motion of the fluids in the effectively two-dimensional radial Hele-Shaw cell problem is described by the gap-averaged Darcy's law [1,2,5]

$$\mathbf{v}_j=-\frac{b^2}{12\eta_j}\boldsymbol{\nabla}p_j, \tag{3}$$

and the gap-averaged incompressibility condition

$$\boldsymbol{\nabla}\cdot\mathbf{v}_j=0, \tag{4}$$

where $\mathbf{v}_j=\mathbf{v}_j(r,\theta)$ and $p_j=p_j(r,\theta)$ are the gap-averaged velocity and pressure of fluid j, respectively, with $j=1,2,3$. Here the subscripts 1, 2, and 3 refer to the inner, intermediate (annulus), and outer fluids, respectively.

The irrotational nature of the flow ($\boldsymbol{\nabla}\times\mathbf{v}_j=0$) allows one to define a velocity potential that obeys the Laplace equation $\nabla^2\phi_j=0$, having the general solution [16,17] (for $j=1,2,3$)

$$\phi_1=-\frac{Q}{2\pi}\ln r+\sum_{n\neq0}\alpha(t)\left(\frac{r}{R_1}\right)^{|n|}e^{in\theta}, \tag{5}$$

$$\phi_2=-\frac{Q}{2\pi}\ln r+\sum_{n\neq0}\delta(t)\left(\frac{r}{R_1}\right)^{-|n|}e^{in\theta}+\sum_{n\neq0}\gamma(t)\left(\frac{r}{R_2}\right)^{|n|}e^{in\theta}, \tag{6}$$

$$\phi_3=-\frac{Q}{2\pi}\ln r+\sum_{n\neq0}\omega(t)\left(\frac{r}{R_2}\right)^{-|n|}e^{in\theta}. \tag{7}$$

In order to describe the dynamics of the trailing and leading interfaces, we have to relate the velocity potential $\phi_j(r,\theta)$ to the position of the interfaces, which is represented, respectively, by $\mathcal{R}_1(\theta,t)$ and $\mathcal{R}_2(\theta,t)$. This can be accomplished by using the kinematic boundary condition, which expresses the fact that the normal components of each fluid velocity are continuous across the interface and that they are equal to the velocity of the interface itself [2]. In our dual-interface spreading problem, this can be written as $(\mathbf{v}_1\cdot\hat{\mathbf{n}})|_{r=\mathcal{R}_1}=(\mathbf{v}_2\cdot\hat{\mathbf{n}})|_{r=\mathcal{R}_1}$ and $(\mathbf{v}_2\cdot\hat{\mathbf{n}})|_{r=\mathcal{R}_2}=(\mathbf{v}_3\cdot\hat{\mathbf{n}})|_{r=\mathcal{R}_2}$. In polar coordinates (r,θ) these two relations are written as

$$\frac{\partial\mathcal{R}_1}{\partial t}=\left(\frac{1}{r^2}\frac{\partial\mathcal{R}_1}{\partial\theta}\frac{\partial\phi_j}{\partial\theta}\right)\bigg|_{r=\mathcal{R}_1}-\left(\frac{\partial\phi_j}{\partial r}\right)\bigg|_{r=\mathcal{R}_1}, \tag{8}$$

for fluids $j = 1, 2$, and

$$\frac{\partial \mathcal{R}_2}{\partial t} = \left(\frac{1}{r^2}\frac{\partial \mathcal{R}_2}{\partial \theta}\frac{\partial \phi_j}{\partial \theta}\right)\bigg|_{r=\mathcal{R}_2} - \left(\frac{\partial \phi_j}{\partial r}\right)\bigg|_{r=\mathcal{R}_2}, \tag{9}$$

for fluids $j = 2, 3$.

The other important boundary condition is the pressure jump at the interface, which is given by the Young-Laplace equation [1,2] for each interface

$$(p_1 - p_2)|_{r=\mathcal{R}_1} = \sigma_{12}\kappa_{12}|_{r=\mathcal{R}_1}, \tag{10}$$

$$(p_2 - p_3)|_{r=\mathcal{R}_2} = \sigma_{23}\kappa_{23}|_{r=\mathcal{R}_2}, \tag{11}$$

where

$$\kappa_{12} = \frac{\mathcal{R}_1^2 + 2\left(\frac{\partial \mathcal{R}_1}{\partial \theta}\right)^2 - \mathcal{R}_1\frac{\partial^2 \mathcal{R}_1}{\partial \theta^2}}{\left[\mathcal{R}_1^2 + \left(\frac{\partial \mathcal{R}_1}{\partial \theta}\right)^2\right]^{3/2}} \qquad \text{and} \qquad \kappa_{23} = \frac{\mathcal{R}_2^2 + 2\left(\frac{\partial \mathcal{R}_2}{\partial \theta}\right)^2 - \mathcal{R}_2\frac{\partial^2 \mathcal{R}_2}{\partial \theta^2}}{\left[\mathcal{R}_2^2 + \left(\frac{\partial \mathcal{R}_2}{\partial \theta}\right)^2\right]^{3/2}}.$$

In Eqs. (10) and (11), κ_{12} and κ_{23} denote the interfacial curvatures on the plane of the cell for the inner and outer interfaces, respectively.

At this point, we have all ingredients needed to derive the set of mode-coupling differential equations for the perturbation amplitudes $\zeta_n(t)$ and $\varepsilon_n(t)$. Following standard steps performed in previous weakly nonlinear studies on Hele-Shaw cells [22,23], we perform Fourier expansions for the velocity potentials [Eqs. (5)–(7)] and use the kinematic boundary condition [Eqs. (8) and (9)] to express the Fourier coefficients of ϕ_j [i.e., $\alpha(t)$, $\delta(t)$, $\gamma(t)$, and $\omega(t)$] in terms of ζ_n and ε_n. Substituting these relations, and the pressure jump condition [Eqs. (10) and (11)] into the Darcy's law [Eq. (3)] and keeping terms up to second-order in ζ and ε, we obtain the set of dimensionless coupled equations of motion for both perturbation amplitudes ζ_n and ε_n (for $n \neq 0$)

$$\dot{\zeta}_n = \underbrace{f_1\left[\frac{|n| - f_1^{-1}}{2\pi R_1^2} - \left(\frac{\beta_{13}\beta_{23}}{\beta_{13} - \beta_{23}}\right)\frac{|n|(n^2-1)}{\mathrm{Ca}R_1^3}\right]\zeta_n + f_2\left[\frac{|n|}{2\pi R_2^2} - \left(\frac{\beta_{23}}{\beta_{23} - 1}\right)\frac{|n|(n^2-1)}{\mathrm{Ca}R_2^3}\right]\varepsilon_n}_{\text{linear}}$$
$$+ \underbrace{\left\{f_1\sum_{n'\neq 0}\left[F(n,n')\zeta_{n'}^{\text{lin}}\zeta_{n-n'}^{\text{lin}} + G(n,n')\dot{\zeta}_{n'}^{\text{lin}}\zeta_{n-n'}^{\text{lin}}\right] + f_2\sum_{n'\neq 0}\left[H(n,n')\varepsilon_{n'}^{\text{lin}}\varepsilon_{n-n'}^{\text{lin}} + I(n,n')\dot{\varepsilon}_{n'}^{\text{lin}}\varepsilon_{n-n'}^{\text{lin}}\right]\right.}$$
$$\left. + f_2\sum_{n'\neq 0}\left[J(n,n')\varepsilon_{n'}^{\text{lin}}\zeta_{n-n'}^{\text{lin}} + K(n,n')\dot{\varepsilon}_{n'}^{\text{lin}}\zeta_{n-n'}^{\text{lin}} + L(n,n')\zeta_{n'}^{\text{lin}}\varepsilon_{n-n'}^{\text{lin}} + M(n,n')\dot{\zeta}_{n'}^{\text{lin}}\varepsilon_{n-n'}^{\text{lin}}\right]\right\}, \tag{12}$$
$$\text{WNL}$$

$$\dot{\varepsilon}_n = \underbrace{f_3\left[\frac{|n|}{2\pi R_1^2} - \left(\frac{\beta_{13}\beta_{23}}{\beta_{13} - \beta_{23}}\right)\frac{|n|(n^2-1)}{\mathrm{Ca}R_1^3}\right]\zeta_n + f_4\left[\frac{|n| - f_4^{-1}}{2\pi R_2^2} - \left(\frac{\beta_{23}}{\beta_{23} - 1}\right)\frac{|n|(n^2-1)}{\mathrm{Ca}R_2^3}\right]\varepsilon_n}_{\text{linear}}$$
$$+ \underbrace{\left\{f_3\sum_{n'\neq 0}\left[\mathcal{F}(n,n')\zeta_{n'}^{\text{lin}}\zeta_{n-n'}^{\text{lin}} + \mathcal{G}(n,n')\dot{\zeta}_{n'}^{\text{lin}}\zeta_{n-n'}^{\text{lin}}\right] + f_4\sum_{n'\neq 0}\left[\mathcal{H}(n,n')\varepsilon_{n'}^{\text{lin}}\varepsilon_{n-n'}^{\text{lin}} + \mathcal{I}(n,n')\dot{\varepsilon}_{n'}^{\text{lin}}\varepsilon_{n-n'}^{\text{lin}}\right]\right.}$$
$$\left. + f_3\sum_{n'\neq 0}\left[\mathcal{J}(n,n')\varepsilon_{n'}^{\text{lin}}\zeta_{n-n'}^{\text{lin}} + \mathcal{K}(n,n')\dot{\varepsilon}_{n'}^{\text{lin}}\zeta_{n-n'}^{\text{lin}} + \mathcal{L}(n,n')\zeta_{n'}^{\text{lin}}\varepsilon_{n-n'}^{\text{lin}} + \mathcal{M}(n,n')\dot{\zeta}_{n'}^{\text{lin}}\varepsilon_{n-n'}^{\text{lin}}\right]\right\}, \tag{13}$$
$$\text{WNL}$$

where lengths and time are rescaled by $R_2(0)$ and $R_2^2(0)/Q$, respectively. Here $\beta_{13} = \eta_3/\eta_1$ ($\beta_{23} = \eta_3/\eta_2$) is the viscosity ratio of fluids 1 and 3 (2 and 3), and

$$\mathrm{Ca} = \frac{12\eta_3 Q R_2(0)}{\sigma b^2} \tag{14}$$

is the capillary number that provides a relative measure of viscous to surface tension forces, assuming that the surface tension coefficients (σ_{12} and σ_{23}) are the same at both interfaces ($\sigma_{12} = \sigma_{23} = \sigma$) [16–21]. In Eqs. (12) and (13),

$$f_1 = \frac{A_{12}(1 - A_{23}R^{2|n|})}{1 + A_{12}A_{23}R^{2|n|}}, \quad f_2 = \frac{A_{23}(1 + A_{12})R^{(|n|-1)}}{1 + A_{12}A_{23}R^{2|n|}},$$
$$f_3 = \frac{A_{12}(1 - A_{23})R^{(|n|+1)}}{1 + A_{12}A_{23}R^{2|n|}}, \quad f_4 = \frac{A_{23}(1 + A_{12}R^{2|n|})}{1 + A_{12}A_{23}R^{2|n|}},$$

where $A_{12} = (\beta_{13} - \beta_{23})/(\beta_{13} + \beta_{23})$ [$A_{23} = (\beta_{23} - 1)/(\beta_{23} + 1)$] is the viscosity contrast of fluids 1 and 2 (2 and 3) written in terms of the viscosity ratios. The ratio of the unperturbed radii

$$R = R(t) = \frac{R_1}{R_2} \tag{15}$$

plays an important role in our system as it measures the coupling strength between the trailing and leading interfaces, and the initial annulus' thickness is written as

$$d = 1 - \frac{R_1(0)}{R_2(0)} = 1 - R_0, \tag{16}$$

where $R_0 = R(t = 0)$. In this way, we can conveniently study the effects of the annulus' thickness by just varying the values of the initial ratio of the unperturbed radii R_0. The linear underbrace terms (i.e., linear in ζ_n and ε_n) on the right-hand sides of Eqs. (12) and (13) reproduce the linear stability analysis first derived by Woods *et al.* [16,17], while the remaining underbrace second-order mode-coupling terms are the contribution that arise as a direct consequence of our weakly nonlinear (WNL) analysis, which considers the presence of a full spectrum of modes. The expressions for the second-order mode-coupling terms are given in the Appendix [see Eqs. (A1)–(A20)].

To contemplate the implications of second-order mode coupling, in Eqs. (12) and (13) we follow Miranda and Widom [22] [see their Eqs. (30)–(32)] and obtain the appropriate segregation between orders in ζ and ε by substituting the purely linear solutions of the mode-coupling differential equations

$$\dot{\zeta}_n^{\mathrm{lin}} = f_1\left[\frac{|n| - f_1^{-1}}{2\pi R_1^2} - \left(\frac{\beta_{13}\beta_{23}}{\beta_{13} - \beta_{23}}\right)\frac{|n|(n^2-1)}{\mathrm{Ca}R_1^3}\right]\zeta_n^{\mathrm{lin}} + f_2\left[\frac{|n|}{2\pi R_2^2} - \left(\frac{\beta_{23}}{\beta_{23} - 1}\right)\frac{|n|(n^2-1)}{\mathrm{Ca}R_2^3}\right]\varepsilon_n^{\mathrm{lin}} \tag{17}$$

and

$$\dot{\varepsilon}_n^{\mathrm{lin}} = f_3\left[\frac{|n|}{2\pi R_1^2} - \left(\frac{\beta_{13}\beta_{23}}{\beta_{13} - \beta_{23}}\right)\frac{|n|(n^2-1)}{\mathrm{Ca}R_1^3}\right]\zeta_n^{\mathrm{lin}} + f_4\left[\frac{|n| - f_4^{-1}}{2\pi R_2^2} - \left(\frac{\beta_{23}}{\beta_{23} - 1}\right)\frac{|n|(n^2-1)}{\mathrm{Ca}R_2^3}\right]\varepsilon_n^{\mathrm{lin}} \tag{18}$$

into the second-order terms appearing on the right-hand side of Eqs. (12) and (13).

Equations (12) and (13) are the coupled second-order mode-coupling expressions of the Saffman-Taylor problem for a radially spreading annulus. Observe that the system is handily described by four controlling physical parameters: R_0, β_{13}, β_{23}, and Ca. While the purely linear differential equations [Eqs. (17) and (18)] provide information about the stability of the dual-interface problem, the nonlinear terms of Eqs. (12) and (13) [given by expressions (A1)–(A20)] offer key insights into the basic morphology of the emerging patterns in the nonlinear regime of the dynamics.

Note that in the limit of a thick annulus ($R \to 0$), the terms multiplied by the functions f_2 [in Eq. (12)] and f_3 [in Eq. (13)] become weak, leaving two decoupled single interfaces. In this case, and after appropriate reintroduction of dimensions, it can be shown that each one of these equations reduces to the considerably simpler expression obtained in Ref. [22] for the corresponding two-fluid (single-interface) version of the problem. On the other hand, in the limit of a thin annulus ($R \to 1$, $R_1 \to R_2$, and $\zeta_n \to \varepsilon_n$) both equations reduce to an expression describing the radial displacement of fluid 3 directly by fluid 1, but with interfacial tension equal to the sum of the interfacial tensions of the two interfaces ($\sigma_{12} + \sigma_{23} = 2\sigma$).

We point out that the theoretical results presented throughout this work are obtained by utilizing parameter values that are consistent with realistic physical quantities related to existing radial Hele-Shaw cell arrangements and material properties of the fluids [2,5–11,16,24–29].

III. EFFECTS OF THE INITIAL ANNULUS' THICKNESS ON NONLINEAR PATTERN-FORMING MECHANISMS

Since the linear aspects of the problem have already been discussed in Refs. [16–21], in this work we focus on the mode-coupling, nonlinear contributions expressed by the WNL terms in Eqs. (12) and (13). An important feature of our second-order perturbative approach is the fact that through the coupling of the appropriate Fourier modes, one is able to extract key analytical information about the morphology of the interface and the finger competition dynamics at the onset of nonlinearities [22].

To begin our discussion, it is convenient to rewrite the net interface perturbation for each of the interfaces [Eqs. (1) and (2)] in terms of cosine and sine modes

$$\zeta(\theta, t) = \zeta_0 + \sum_{n=1}^{\infty} [a_n(t)\cos(n\theta) + \overline{a}_n(t)\sin(n\theta)], \tag{19}$$

$$\varepsilon(\theta, t) = \varepsilon_0 + \sum_{n=1}^{\infty} \left[b_n(t)\cos(n\theta) + \overline{b}_n(t)\sin(n\theta)\right], \tag{20}$$

where for a given mode $a_n(t) = \zeta_n(t) + \zeta_{-n}(t)$ [$b_n(t) = \varepsilon_n(t) + \varepsilon_{-n}(t)$] and $\overline{a}_n = i(\zeta_n - \zeta_{-n})$ [$\overline{b}_n = i(\varepsilon_n - \varepsilon_{-n})$] denote the real-valued cosine and sine amplitudes, respectively. Without loss of generality, as in Ref. [22] we may choose the phase of the fundamental modes so that $a_n > 0$, $b_n > 0$ and $\overline{a}_n = \overline{b}_n = 0$. Unlike the purely linear regime where $\zeta_0 = \varepsilon_0 = 0$, the terms ζ_0 and ε_0 in Eqs. (19) and (20) express an intrinsically nonlinear concern because they consist of a second-order correction in ζ and ε, respectively.

The most representative pattern-forming mechanisms of the viscous fingering instability in injection-driven Hele-Shaw flows can be identified as spreading, splitting, and competition [2]. Some time ago, it was shown that these basic nonlinear morphological mechanisms could be consistently reproduced by considering the weakly nonlinear coupling of just a few participating modes [22,23]: the characteristic shape of the fingers (e.g., finger-tip widening, splitting, and sharpening behaviors) could be given by the interplay between the fundamental mode n and its first-harmonic cosine mode $2n$, while finger competition events (or finger length variability) could be described by the interaction of a fundamental mode n and its sine and cosine subharmonic modes $n/2$. Here we use this simple picture in order to get some insight into the morphology and early nonlinear features of the patterns generated in our two-interface system. It should be stressed that the effectiveness of this particular weakly nonlinear strategy has been amply substantiated by a number of analytical, numerical, and experimental studies in the Hele-Shaw flow literature (see, for instance, Refs. [30–38]).

On the basis of these simple mode-coupling fingering mechanisms, in the following we consider the nonlinear coupling of the appropriate representative modes and analyze how the controlling

parameters of our system (R_0, β_{13}, β_{23}, and Ca) contribute to the time evolution and the shapes of the interfaces.

A. Inner interface unstable ($\eta_1 < \eta_2$) and outer interface stable ($\eta_2 > \eta_3$)

1. The shape of the fingers

Considering the importance of the finger-tip splitting phenomena for Hele-Shaw flows, one interesting point is to find out if the fingers would tend to be more wide or narrow as the annulus' thickness is varied. We are particularly interested in understanding how the initial annulus' thickness, as well as the capillary number Ca, influence the mechanisms of finger-tip broadening, splitting, and sharpening for both interfaces. This is examined considering two distinct cases: in the first case, fluid viscosities are chosen as such that the inner interface is unstable while the outer is stable (Sec. III A), and then the opposite situation where the inner interface is stable and the outer one is unstable (Sec. III B).

Within the scope of our mode-coupling theory, it has been shown that finger-tip widening, splitting, and sharpening are behaviors related to the influence of a fundamental mode n on the growth of its harmonic mode $2n$ [22]. In other words, it has been demonstrated that these basic pattern-forming phenomena can be predicted, captured, and properly described already at second order in the perturbation amplitudes, and by considering the nonlinear coupling between just two Fourier modes, namely, n and $2n$. Therefore, to tackle finger-tip morphologies at the weakly nonlinear level, we rewrite Eqs. (19) and (20) in terms of these two morphologically relevant Fourier modes

$$\zeta(\theta, t) = \zeta_0 + a_n(t)\cos(n\theta) + a_{2n}(t)\cos(2n\theta), \tag{21}$$

$$\varepsilon(\theta, t) = \varepsilon_0 + b_n(t)\cos(n\theta) + b_{2n}(t)\cos(2n\theta). \tag{22}$$

It is apparent from Eqs. (21) and (22) that to describe the time evolution of the perturbed interfaces $\mathcal{R}_1(\theta, t)$ and $\mathcal{R}_2(\theta, t)$, one needs to know how the cosine amplitudes $a_n(t)$, $a_{2n}(t)$, $b_n(t)$, and $b_{2n}(t)$ evolve in time. To do that, we rewrite the set of mode-coupling equations (12) and (13) in terms of the real-valued cosine amplitudes, considering the interplay of modes n and $2n$. Then the time evolution of such mode amplitudes can be obtained by numerically solving the corresponding coupled nonlinear differential equations. Once this is done, the shape of the evolving interfaces can be easily acquired by using Eqs. (21) and (22).

It has been shown [22] that an enhanced tendency of the outward-moving fingers of fluid 1 to get wider (narrower) occurs when $a_{2n} < 0$ ($a_{2n} > 0$). So a negative growth for the cosine amplitude of the first harmonic mode $2n$ would mean a tendency for the fingers of the inner trailing interface to be wide and flat at their tips, favoring the development of finger-tip splitting events. On the other hand, a positive growth for the cosine amplitude $2n$ reverses the above conclusions, that is, results in the development of narrow outward-pointing fingers of the inner interface, and thus promoting finger-tip sharpening phenomenon. The morphology of the outer leading interface can be described in a very similar way, but analyzing the growth of the cosine amplitude b_{2n}. This weakly nonlinear mode-coupling description is able to extract key morphological aspects of the inner and outer interfaces already at lowest nonlinear order (i.e., at second order in ζ and ε).

In Fig. 2 we illustrate the typical weakly nonlinear morphologies that may emerge in the dual-interface radial Hele-Shaw flows when $\eta_1 < \eta_2$ and $\eta_2 > \eta_3$. In the top panels, we plot the shape of the two expanding interfaces for four increasing values of parameter R_0: (a) $R_0 = 0.05$, (b) $R_0 = 0.2$, (c) $R_0 = 0.3$, and (d) $R_0 = 0.37$. In the bottom panels of Fig. 2, for each value of R_0, we depict the time evolution of the rescaled perturbation amplitudes $a_n(t)/R_1(t)$, $a_{2n}(t)/R_1(t)$, $b_n(t)/R_2(t)$, and $b_{2n}(t)/R_2(t)$ for the participating modes $n = 4$ and $2n = 8$, without loss of generality. All patterns illustrated in Fig. 2 have the same initial amplitudes $a_n(0) = b_n(0) = 2 \times 10^{-4}$ and $a_{2n}(0) = b_{2n}(0) = 0$. By applying such initial conditions we guarantee that the phenomena of finger-tip splitting, broadening, and narrowing are spontaneously induced by the weakly nonlinear

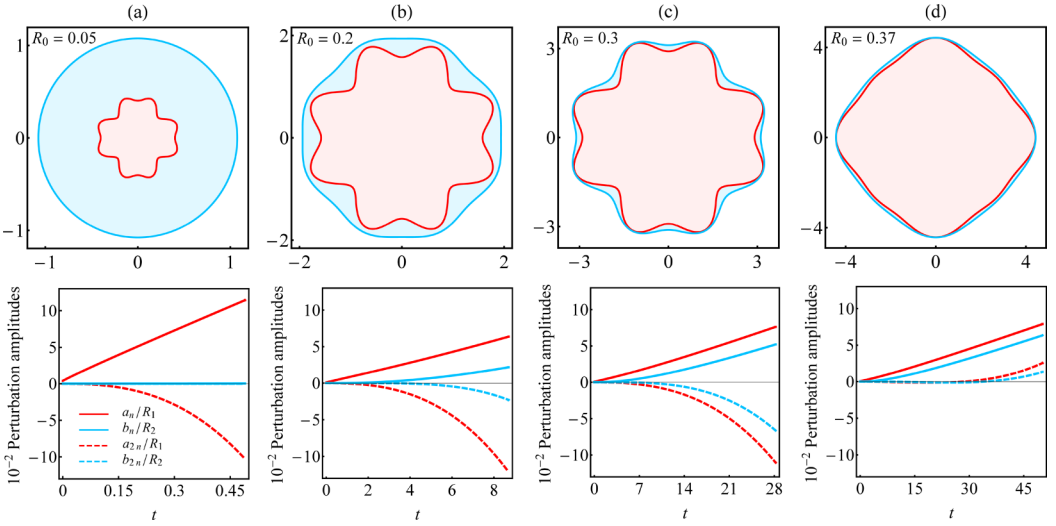

FIG. 2. Snapshot of the weakly nonlinear interfaces (top panels), illustrating typical fingering patterns during three-layer radial Hele-Shaw flows in which the trailing fluid-fluid interface is unstable and the leading interface is stable. The corresponding time evolution of the rescaled cosine perturbation amplitudes $a_n(t)/R_1(t)$, $b_n(t)/R_2(t)$, $a_{2n}(t)/R_1(t)$, and $b_{2n}(t)/R_2(t)$ for modes n and $2n$, where $n = 4$, is depicted in the bottom panels. The values taken for the initial ratio of the unperturbed radii are (a) $R_0 = 0.05$, (b) $R_0 = 0.2$, (c) $R_0 = 0.3$, and (d) $R_0 = 0.37$. In addition, we set $\beta_{13} = 33\,300$, $\beta_{23} = 0.6$, $\mathrm{Ca} = 5000$, and the final times used are (a) $t_f = 0.49$, (b) $t_f = 8.70$, (c) $t_f = 28.22$, and (d) $t_f = 50.16$.

terms of Eqs. (12) and (13), and not by artificially imposing large initial amplitudes for a_{2n} and b_{2n}. In addition, we take $\beta_{13} = 33\,300$, $\beta_{23} = 0.6$, and $\mathrm{Ca} = 5000$.

The patterns shown in Fig. 2 have been obtained after time has evolved in the interval $0 \leqslant t \leqslant t_f$. It should be stressed that the values of the final times t_f used in Fig. 2, and in other parts of this work are not arbitrary. To determine t_f, we follow an approach originally proposed by Gingras and Rácz [39] for the linear regime, and we extend its range of applicability to the weakly nonlinear stage of evolution. While plotting the interfaces depicted in this paper, we stop the time evolution of the interfaces as soon as the base of the fingers starts to move inwards, which would make successive interfaces cross one another. This criterion for determining t_f is justified by the fact that the crossing of successive time evolving interfaces (i.e., the occurrence of backward interface motion) is detected neither in experiments [2,5,9] nor in numerical simulations [12–14,40–42] of radial Hele-Shaw flows. Therefore, we adopt $t = t_f$ as the upper bound time for the validity of our perturbative approach. In Fig. 2 the inner trailing interface is always more unstable than the outer leading interface and, therefore, present occurrence of backward motion of the base of the fingers before the outer interface. In this framework, and within the scope of our mode-coupling theory, t_f is set as the instant when the velocity of the inner interface becomes negative for the first time. This validity condition can be mathematically expressed as

$$\left[\frac{d\mathcal{R}_1}{dt}\right]_{t=t_f} = [\dot{R}_1(t) + \dot{\zeta}(\theta, t)]_{t=t_f} = 0, \tag{23}$$

where Eq. (23) is evaluated by using our weakly nonlinear mode-coupling equations (12) and (13).

Now we initiate our discussion by surveying Fig. 2(a), which considers the situation of a very thick annulus ($R_0 = 0.05$). We observe a inner interface presenting a four-fingered structure determined by the growth of the fundamental mode $n = 4$. It is clear that each of these fingers bifurcate at their tips and the classical finger-tip splitting phenomenon can be identified. Recall

that finger-splitting morphology is generated by the negative growth of the first harmonic mode $2n$ ($a_{2n} < 0$). We do verify this behavior in the bottom panel of Fig. 2(a), where a_{2n} evolves as negative values. On the other hand, by examining the outer interface in the top panel of Fig. 2(a), one immediately verifies that for such a low value of parameter R_0, the leading interface exhibits a nearly circular shape with negligible disturbances, as quantified in the corresponding bottom panel of Fig. 2(a). Therefore, when $R_0 = 0.05$, the coupling between the interfaces is very weak and, although the inner interface evolves to a fingered pattern presenting bifurcated fingers of sizable length, this is not enough to induce the development of disturbances on the outer stable interface.

In Fig. 2(b) we set $R_0 = 0.2$. Despite the fact that the inner interface remains almost identical to the previous situation ($R_0 = 0.05$), perhaps just presenting a slightly enhancement of the finger tip-splitting phenomenon followed by a reduction on the overall size of the pattern, for this higher value of R_0, one notices the formation of modestly deformed fingers having small perturbation amplitudes on the outer interface. Although no finger-tip splitting events are observed, the outward-moving fingers of the outer interface are wide and flat at their tips, characterizing the onset of tip-splitting phenomenon. These visual findings are in agreement with quantification of all modes in the bottom panel of Fig. 2(b), where one can see that these suggestive morphological events are due to the growth of both perturbation amplitudes b_n and b_{2n}, which now have, respectively, sizable positive and negative magnitudes. Also, the perturbation amplitudes related to the outer interface (b_n and b_{2n}) are smaller in magnitude than the amplitudes of the inner interface (a_n and a_{2n}). For this reason, the inner interface exhibits a fingered pattern presenting longer bifurcated fingers, while the outer interface is just modestly deformed.

An even more revealing morphological behavior is observed in Fig. 2(c), where $R_0 = 0.3$. By inspecting the interfaces, we notice the evolution of broadened, two-lobe shaped fingers, clearly showing bifurcated tips on both inner and outer interfaces. Note that the shape of each interface almost matches one another. Such a curious pattern-forming behavior can be justified by resorting to our mode-coupling approach: from the bottom panel of Fig. 2(c) one can see that this scenario is promoted by the enhanced nonlinear growth of the perturbation amplitudes b_n and b_{2n}, which now are not only higher in magnitude than the corresponding situation depicted in Fig. 2(b), but actually are approaching the amplitudes of the inner interface a_n and a_{2n}.

If we keep increasing the value of the parameter R_0, i.e., a thinner fluid annulus, we observe first a less prominent growth for the mode $2n$ (which, incidentally, become less negative) and then a change in the sign of that mode [for instance, for $R_0 = 0.37$, as in Fig. 2(d)], so both a_{2n} and b_{2n} become positive. Recall that this is precisely the sign of $2n$ that favors the formation of narrow fingers [22]. As a consequence, instead of broadened and split fingers [as illustrated in Figs. 2(a)–2(c)], in Fig. 2(d) one observes the formation of a polygonal-like, fourfold patterns, presenting sharpened fingers. It's worthwhile to note that the final shapes of both interfaces are very similar and almost indistinguishable. Hence, when $R_0 = 0.37$, the coupling between the interfaces is strong and they evolve almost as a single interface with matched shapes. In addition, as opposed to what occurred in Figs. 2(a)–2(c), finger-tip widening and splitting are not detected in Fig. 2(d).

It is worthwhile to point out that the finger-tip widening, splitting, and sharpening phenomena detected in Fig. 2 are inherently nonlinear and could not be either predicted or captured by a purely linear perturbative description of the three-layer radial Hele-Shaw problem. To illustrate this important point, in Fig. 3 we plot the linear interface shapes by using the same physical parameters and initial conditions as those used in Fig. 2. The only difference between Figs. 2 and 3 is that, while Fig. 3 is obtained by numerically solving the purely linear (in ζ and ε) Eqs. (17) and (18), Fig. 2 results from the numerical solution of the second-order $[O(\zeta^2)]$ and $[O(\varepsilon^2)]$ mode-coupling equations (12) and (13). By contrasting the patterns shown in Fig. 2 and in Fig. 3, we note that the linear patterns are structureless as compared to their nonlinear counterparts. At the linear level, the participating Fourier modes n decouple [as expressed by Eqs. (17) and (18)] and the basic mode-coupling ingredients are completely absent. As a result, the shape of the patterns illustrated in Fig. 3 is dominated by the growth of fundamental mode n only. On the other hand, the weakly nonlinear morphologies revealed in Fig. 2 emerge due to the coupling and enhanced nonlinear

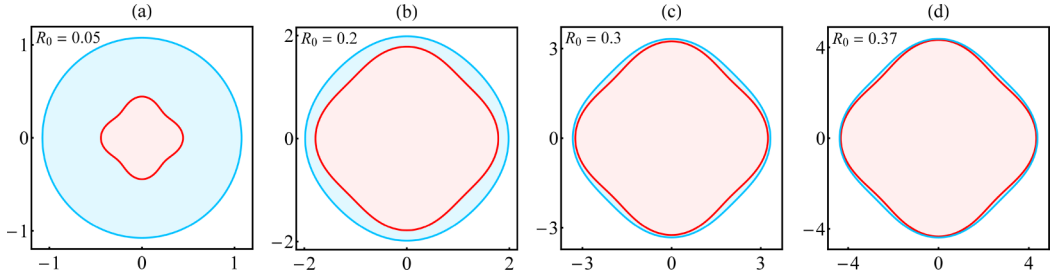

FIG. 3. Fingering patterns obtained by using the purely linear dynamic description of the problem. These linear patterns [obtained by utilizing the set of Eqs. (17) and (18)] should be contrasted with the equivalent weakly nonlinear pattern-forming structures illustrated in Figs. 2(a)–2(d) which have been generated by employing our second-order mode-coupling scheme [by using the set of Eqs. (12) and (13)]. All physical parameters and initial conditions used here are identical to those utilized in Fig. 2.

growth of modes n and $2n$. As consequence of this nontrivial nonlinear coupling among the fundamental mode n and its first harmonic $2n$, the corresponding weakly nonlinear forms shown in Fig. 2 unveil the development of much richer finger-tip configurations [wide and blunt/bifurcated as in Fig. 2(b), or narrow and sharpened as depicted in Fig. 2(d)]. These findings reinforce the necessity of including the nonlinear interaction among participating modes in order to get a more elaborate morphological elements to the three-layer radial Hele-Shaw fingering patterns via a perturbative scheme.

Supplementary information about the changes occurring in the finger shapes for both the inner and outer interfaces when the parameter R_0 is varied is provided by Fig. 4. By using the very same set of physical parameters and initial conditions utilized in Fig. 2, Fig. 4 illustrates parametric plots expressing the behavior of the ratios (a) $b_n(t)/R_2(t)$, (b) $b_{2n}(t)/R_2(t)$, and (c) $a_{2n}(t)/R_1(t)$ with respect to variations in $a_n(t)/R_1(t)$ as time advances, for the situations depicted in Fig. 2. This is done for two distinct capillary numbers $\mathrm{Ca} = 5000$ (solid curves) and $\mathrm{Ca} = 6000$ (dashed curves).

The type of graph portrayed in Fig. 4 is convenient to contrast the morphologies that arise in Fig. 2 for each value of R_0, since the ratio $a_n(t)/R_1(t)$ [$b_n(t)/R_2(t)$] is related to the average size and overall n-fold symmetry of the inner (outer) patterned structure, while $a_{2n}(t)/R_1(t)$ [$b_{2n}(t)/R_2(t)$] determines the typical morphology of the finger tip (i.e., if the tips are wide and split, or if they are narrow and get sharper) for the inner (outer) interface. Recall that is essentially the development of

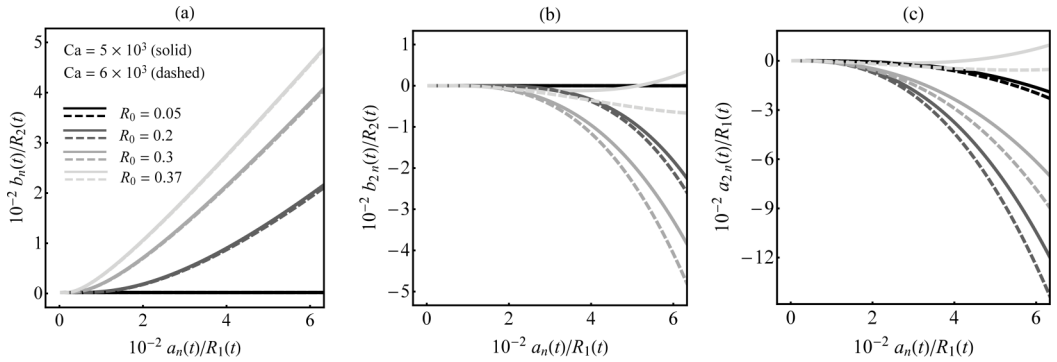

FIG. 4. Parametric plot expressing the behavior of (a) $b_n(t)/R_2(t)$, (b) $b_{2n}(t)/R_2(t)$, and (c) $a_{2n}(t)/R_1(t)$ with respect to variations in $a_n(t)/R_1(t)$, for four values of initial ratio of the unperturbed radii R_0 and two values of capillary number Ca. All physical parameters and initial conditions are the same as the ones used in Fig. 2.

the unstable inner interface [related to the ratio $a_n(t)/R_1(t)$] that induces the growth of disturbances on the outer interface. For that reason, we choose to analyze the behavior of the ratios $b_n(t)/R_2(t)$, $b_{2n}(t)/R_2(t)$, and $a_{2n}(t)/R_1(t)$ with respect to $a_n(t)/R_1(t)$.

First, by examining Fig. 4(a), it is apparent that, except for $R_0 = 0.05$, the rescaled amplitude $b_n(t)/R_2(t)$ increases when $a_n(t)/R_1(t)$ assumes larger values. It's also clear that, for any given value of $a_n(t)/R_1(t)$, larger values of R_0 are related to greater magnitudes of the rescaled amplitude $b_n(t)/R_2(t)$, as indicated by the solid curves. These results seem not to be significantly influenced by changing the capillary number, as the dashed curves are almost superposed to the solid ones. Therefore, our findings suggest that larger values of R_0 (i.e., thinner fluid annulus) lead to outer interfaces with greater overall sizes.

Now we turn to Fig. 4(b), which focuses on the behavior of $b_{2n}(t)/R_2(t)$ with respect to variations in $a_n(t)/R_1(t)$. First, for $R_0 = 0.05$, we observe that $b_{2n}(t)/R_2(t)$ is zero and does not change as $a_n(t)/R_1(t)$ increases. Furthermore, for $R_0 = 0.2$ and $R_0 = 0.3$, the solid curves show a tendency to $b_{2n}(t)/R_2(t)$ becomes negative. This is precisely the phase of the harmonic that favors finger-tip widening and tip splitting of the outward-moving fingers of the leading interface. However, if we keep increasing the value of the initial ratio of the unperturbed radii up to $R_0 = 0.37$, the magnitude of the rescaled perturbation amplitude $b_{2n}(t)/R_2(t)$ is not only attenuated, but starts to grow with a positive phase. In the framework of our weakly nonlinear analysis, a positive phase of the harmonic favors the formation of narrow fingers on the outer interface. As illustrated by the dashed curves, a larger value of capillary number Ca tends to enhance the finger-tip widening and tip splitting events for all values of $R_0 \neq 0.05$, that is, leads to more negative values of b_{2n}. Curiously, this nonlinear effect is observed even for $R_0 = 0.37$, where the magnitude of b_{2n} is positive for lower values of Ca.

Last, we investigate Fig. 4(c), which illustrates the growth of the ratio $a_{2n}(t)/R_2(t)$ with respect to $a_n(t)/R_1(t)$. Similar to the behavior of $b_{2n}(t)/R_2(t)$ [depicted in Fig. 4(b)], $a_{2n}(t)/R_2(t)$ also grows negatively as $a_n(t)/R_1(t)$ increases, for lower values of R_0 ($R_0 = 0.05$ and $R_0 = 0.2$). It's clear that the growth of $a_{2n}(t)/R_2(t)$ is restrained for $R_0 = 0.3$ and changes from negative to positive growth when larger values of R_0 are considered (for instance, $R_0 = 0.37$). Again, a larger value of capillary number leads to more negative values of a_{2n}. The observations extracted from Fig. 4 are consistent with the equivalent interfacial patterns behaviors plotted in Fig. 2 and quantitatively support our weakly nonlinear findings.

Figure 2 revealed that, when we consider larger values of the parameter R_0 and a fixed Ca, a change in the morphology of both the inner and outer interfacial patterns is observed: broader fingers with bifurcated tips are replaced by narrower sharpened ones. This is induced by the change in the sign of the first harmonic $2n$ (a_{2n} and b_{2n}). With this fact in mind, we close this section by examining Fig. 5 that presents a morphological phase diagram for the emerging patterns in the parameter space (Ca, R_0). The representative interfacial patterns shown in Fig. 5 are plotted for $\beta_{13} = 33\,300$, $\beta_{23} = 0.6$, and for the same initial perturbation amplitudes used in Fig. 2. In such a diagram we can identity the establishment of two different morphological regions, separated by a dashed line: the first region (located below the dashed line) is characterized to the occurrence of viscous fingering patterns exhibiting wider fingers with blunt tips (which occurs for $a_{2n} < 0$ and $b_{2n} < 0$), which may start to bifurcate by splitting at their tips. Conversely, the region located above the dashed line is typified by the appearance of a different type of viscous fingering shapes, polygonal-like structures, having shorter sharpened fingers (which arise for $a_{2n} > 0$ and $b_{2n} > 0$). The dashed line separating the regions in Fig. 5 is obtained by evaluating the range of values for the parameters Ca and R_0 such that the first harmonic amplitude for the inner interface is equal to zero [$a_{2n}(t_f) = 0$], for the final time $t_f = 50.16$.

The detection of this transition from finger widening to sharpening that takes place at larger values of R_0 is somewhat surprising. Such behavior is not commonly seen in experiments and numerical simulations of the single-interface two-fluid radial Hele-Shaw flow [3–15], in which the finger-tip broadening/splitting regime is evident. However, in the presence of a third layer of fluid the nonlinear coupling between the interfaces leads to this curious regime where finger-tip sharpening events suppress the conventional finger-tip widening regime. This is quite intriguing.

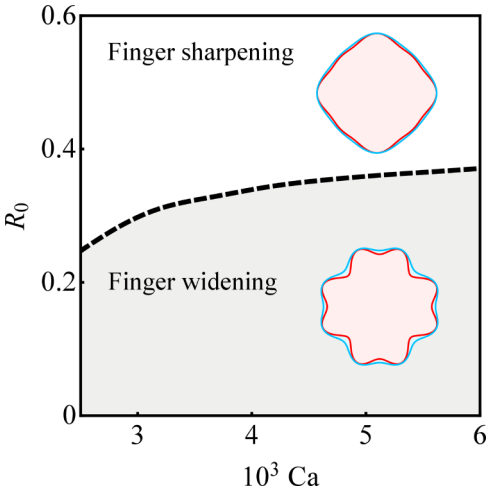

FIG. 5. Morphological phase diagram in the parameter space (Ca, R_0). The dashed line delimitates the boundary between the two different morphological regions. The development of viscous fingering patterns is observed in both regions, where either finger widening or finger sharpening may occur. Here we take $\beta_{13} = 33\,300$, and $\beta_{23} = 0.6$.

Although our weakly nonlinear approach does reveal a positive growth of the first harmonics a_{2n} and b_{2n} for larger values of R_0, lamentably, at this point, we do not have a good physical explanation for this fact. Therefore, the understanding of the physical mechanism leading to this transition in our system remains an open question.

2. Finger competition behavior

Now we turn our attention to the effects of R_0 on finger competition events. Once again, we follow Ref. [22] and consider finger length variability as a measure of the competition among fingers. Within our approach the finger competition mechanism can be described by the influence of a fundamental mode n, assuming n is even, on the growth of its sine and cosine subharmonic modes $n/2$. Therefore, we rewrite Eqs. (19) and (20) as

$$\zeta(\theta, t) = \zeta_0 + a_n(t)\cos(n\theta) + a_{n/2}(t)\cos(n\theta/2) + \overline{a}_{n/2}(t)\sin(n\theta/2), \tag{24}$$

$$\varepsilon(\theta, t) = \varepsilon_0 + b_n(t)\cos(n\theta) + b_{n/2}(t)\cos(n\theta/2) + \overline{b}_{n/2}(t)\sin(n\theta/2). \tag{25}$$

The action of the subharmonic mode breaks the n-fold rotational symmetry of the fundamental by alternately increasing and decreasing the length of each of the n fingers. In Ref. [22] it has been shown that, under injection-driven radial Hele-Shaw flow cosine mode $a_{n/2}$ grows, and sine mode $\overline{a}_{n/2}$ decays. The result is an increased variability among the lengths of the outward moving fingers of fluid 1 invading fluid 2, as observed in actual two-fluid single-interface radial Hele-Shaw flows [5–11]. In the framework of our two-interface system, this effect describes the preferential and more intense competition among outward moving fingers of the trailing inner interface. Likewise, one can extract information about the competition dynamics of the fingers of the outer leading interface by analyzing the behavior of the perturbation amplitudes $b_{n/2}$ and $\overline{b}_{n/2}$. This candid mechanism mimics the actual finger competition phenomenon observed in laboratory and numerical experiments of Hele-Shaw flows. It is worth noting that the validity and correctness of this finger competition mechanism for advanced time stages of the Hele-Shaw cell dynamics has already been tested by extensive numerical simulations [34,35].

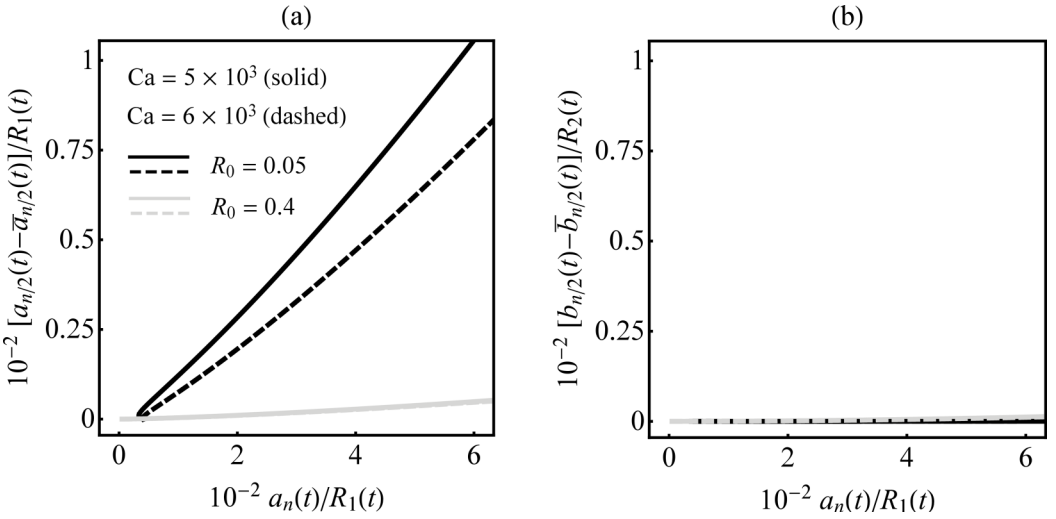

FIG. 6. Parametric plot expressing the behavior of (a) $[a_{n/2}(t)/R_1(t) - \overline{a}_{n/2}(t)/R_1(t)]$ and (b) $[b_{n/2}(t)/R_2(t) - \overline{b}_{n/2}(t)/R_2(t)]$ with respect to variations in $a_n(t)/R_1(t)$, for two values of initial ratio of the unperturbed radii R_0 and two values of capillary number Ca.

To exemplify a characteristic impact of the initial annulus' thickness on the finger competition behavior, Fig. 6 illustrates parametric plots of the difference between the rescaled cosine and sine perturbation amplitudes for the subharmonic modes (a) $[a_{n/2}(t)/R_1(t) - \overline{a}_{n/2}(t)/R_1(t)]$ and (b) $[b_{n/2}(t)/R_2(t) - \overline{b}_{n/2}(t)/R_2(t)]$, relative to the amplitude of the rescaled fundamental mode $a_n(t)/R_1(t)$. This kind of plot is convenient in the sense that it simultaneously expresses the behavior of both $a_{n/2}(t)$ and $\overline{a}_{n/2}(t)$ [$b_{n/2}(t)$ and $\overline{b}_{n/2}(t)$], which are responsible for the finger competition mechanism of the inner (outer) interface, with respect to the growth of the fingers of the inner interface as a whole (provided by the fundamental mode). In Fig. 6 we set the values $R_0 = 0.05$ and $R_0 = 0.4$, and two distinct capillary numbers $\mathrm{Ca} = 5.0 \times 10^3$ (solid curves) and 6×10^3 (dashed curves). In addition, we set $\beta_{13} = 33\,300$ and $\beta_{23} = 0.6$. The initial conditions are taken as $a_n(0) = b_n(0) = 2 \times 10^{-4}$ and $\overline{a}_{n/2}(0) = \overline{b}_{n/2}(0) = 1.67 \times 10^{-4}$, and we consider the interaction of the fundamental mode $n = 8$, and its subharmonic $n/2 = 4$.

From Fig. 6(a), first, we verify that the difference $[a_{n/2}(t)/R_1(t) - \overline{a}_{n/2}(t)/R_1(t)]$ increases when the amplitude of the fundamental mode $a_n(t)/R_1(t)$ assumes larger values. It turns out that, within the scope of our mode-coupling description, this is precisely the behavior of the subharmonic modes that favors outward finger competition of the inner interface (i.e., prevalence of the growth of $a_{n/2}$ over the growth of $\overline{a}_{n/2}$). In addition, for any given value of $a_n(t)/R_1(t)$, it is evident that when $R_0 = 0.05$, $[a_{n/2}(t)/R_1(t) - \overline{a}_{n/2}(t)/R_1(t)]$ is larger than for $R_0 = 0.4$. This observation suggests that, when the initial annulus' thickness is decreased and the interfaces are strongly coupled, nonlinear effects attenuate competition events of the outward fingers of the inner interface. Now, we turn our attention to Fig. 6(b) and analyze the behavior of $[b_{n/2}(t)/R_2(t) - \overline{b}_{n/2}(t)/R_2(t)]$. Here we observe that for $R_0 = 0.05$ there is no finger competition among the outward fingers of the outer interface. This is expected since for such a low value of R_0 there is no growth of disturbances on the outer interface, as shown by Figs. 2(a), 3(a), and 4(a). Nevertheless, if one considers a larger value $R_0 = 0.4$, the difference $[b_{n/2}(t)/R_2(t) - \overline{b}_{n/2}(t)/R_2(t)]$ is just slightly positive even though for that value of R_0 the outer interface exhibits finger development. These findings indicate that when fingers occur on the outer interface due to the coupling with the inner interface, these fingers exhibit similar lengths and competition events are nearly absent. Lastly, by inspecting Fig. 6 an interesting aspect of the nonlinear dynamics can be observed: a larger value of Ca leads to a relatively modest inhibition

of the outward finger competition. This curious weakly nonlinear theoretical result regarding the role of capillary effects on finger length variability behavior has also been observed in single-interface lifting Hele-Shaw cell studies [43,44].

B. Inner interface stable ($\eta_1 > \eta_2$) and outer interface unstable ($\eta_2 < \eta_3$)

In this section we study the role played by the annulus' thickness on the development of the dual-interface radial fingering in Hele-Shaw cells, under a physical situation where the inner trailing interface is stable ($\eta_1 > \eta_2$) and the outer leading interface has an unstable viscosity jump ($\eta_2 < \eta_3$). This case is precisely the opposite of the situation analyzed previously in Sec. III A.

In order to assess key information about the morphology of the arising patterns under the presence of the fluid annulus, we again turn to the weakly nonlinear dynamics. This is done in Fig. 7, where we plot in the top panels the shape of the two interfaces and, similar to Fig. 2, in the bottom panels we depict the time evolution of the rescaled cosine amplitudes $a_n(t)/R_1(t)$, $b_n(t)/R_2(t)$, $a_{2n}(t)/R_1(t)$, and $b_{2n}(t)/R_2(t)$ for modes n and $2n$. The initial conditions are $a_n(0) = b_n(0) = 2 \times 10^{-4}$ and $a_{2n}(0) = b_{2n}(0) = 0$.

In opposition to the rich fingering dynamics identified in Sec. III A and illustrated by Figs. 2–6, here we do not observe a strong influence of the parameters R_0 and Ca on the final shapes of the inner and outer interfaces. Therefore, instead of systematically analyze the effects of changes in R_0 and Ca (as we did in Sec. III A), in Fig. 7 we search for other interesting types of pattern-forming structures by varying all the physical parameters of the system. Moreover, here we do not investigate finger competition behavior since there are no clear signs of competition in the experiments conducted in Ref. [16]. We stress that the patterns illustrated in Figs. 7(a) and 7(b) are generated considering a completely different set of physical parameters, and they should not be directly compared as if they correspond to the same physical situation.

That being said, we begin our discussion by examining Fig. 7(a). In this figure we plot the interfaces by considering the set of physical parameters: $R_0 = 0.1$, $\beta_{13} = 0.6$, $\beta_{23} = 33\,300$, Ca $=$ 5000, and $t_f = 15.95$. Here $n = 9$ is chosen as the fundamental mode. We would like to emphasize that other choices of unstable Fourier modes as being the fundamental mode at $t = 0$ would lead to results very similar to the ones obtained for $n = 9$. From the interfaces depicted at the final time t_f in the top panel, one readily verifies that the inner interface is apparently stable and no growing perturbation is visible. As for the outer unstable interface, we may verify the development of a wavelike pattern presenting fingers with flat tips. These pictorial conclusions are supported by the complementary results presented in the bottom panel of Fig. 7(b), where the rescaled amplitudes $a_n(t)/R_1(t)$ and $a_{2n}(t)/R_1(t)$ are zero and do not change as time progresses. On the other hand, one can see that $b_n(t)/R_2(t)$ [$b_{2n}(t)/R_2(t)$] grows with positive (negative) phase and therefore we should expect an outer interface exhibiting blunt fingers.

Note that, at the final time of the plots of Fig. 7(a), the base of the fingers of the outer leading interface merge with the circular inner interface. In Hele-Shaw flows performed in a similar circumstances to the one presented here, it has been shown experimentally by Cardoso and Woods in Ref. [16] that, for subsequent times, the intermediate fluid annulus break up into drops (see their Fig. 19) and eventually separate due the action of the surface tension, which tends to smooth point edges at the rear at the moment of rupture. Of course the rupture of the fluid annulus and the subsequent formation of drops are beyond the capability of our analytical weakly nonlinear theory. Nonetheless, by inspecting the patterns displayed in the top panel of Fig. 7(a), we can say that our analytical model captures the onset of the formation of drops and our weakly nonlinear findings are consistent with the advance-time experiments performed in Ref. [16].

In Fig. 7(b) the patterns are plotted for $R_0 = 0.2$, $\beta_{13} = 300$, $\beta_{23} = 1000$, Ca $= 5000$, and $t_f = 180.75$. Also, $n = 4$ is set as the fundamental mode. The scenario reviled by the top panel of Fig. 7(b) is quite unexpected. It's apparent that both interfaces are not very much distorted from a perfectly circular shape at the final time t_f considered here. Although the magnitude of the rescaled perturbation amplitudes $a_n(t)/R_1(t)$ and $a_{2n}(t)/R_1(t)$ of the inner interface are smaller than other

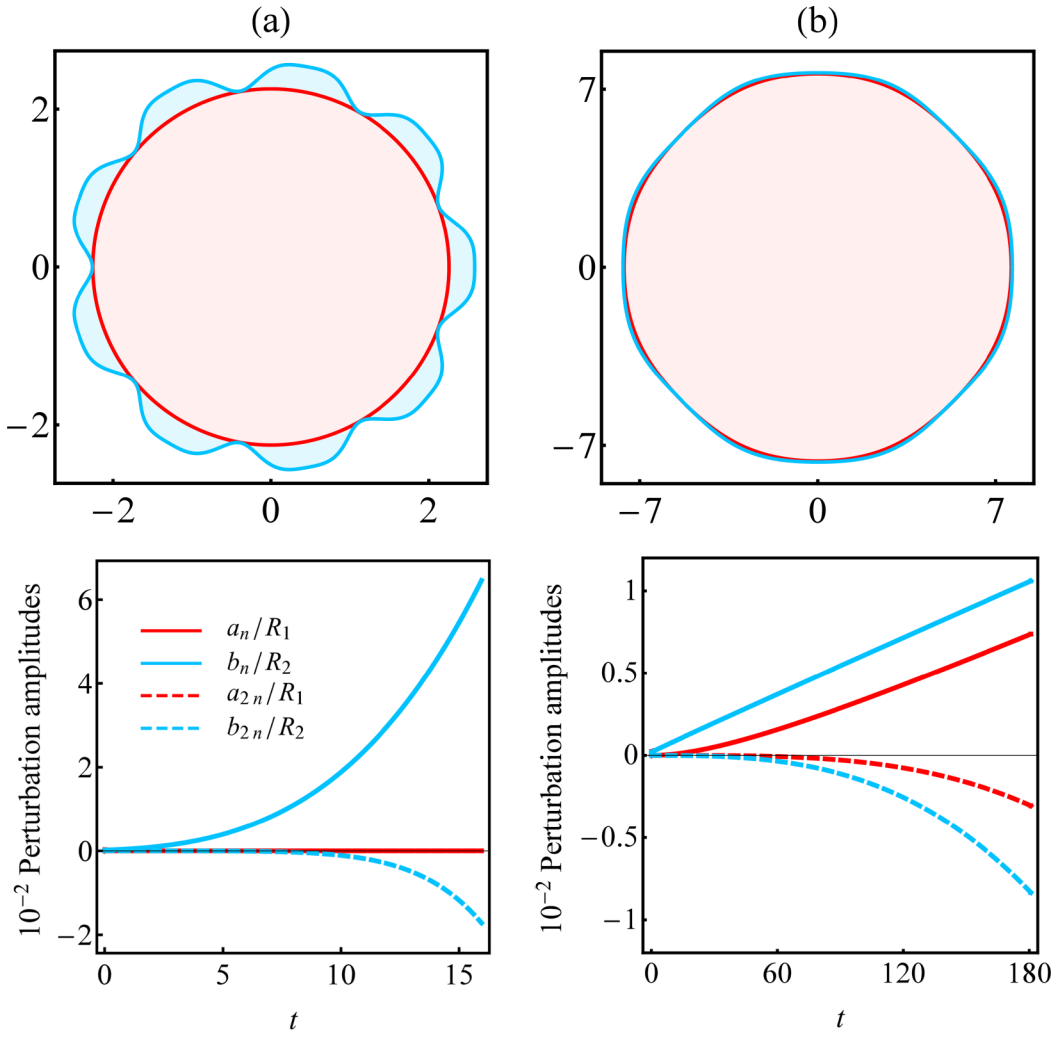

FIG. 7. Snapshot of the weakly nonlinear interfaces (top panels), illustrating typical fingering patterns during three-layer radial Hele-Shaw flows. In contrast to the situation depicted in Fig. 2, here the leading fluid-fluid interface is unstable. The corresponding time evolution of the rescaled cosine perturbation amplitudes $a_n(t)/R_1(t)$, $b_n(t)/R_2(t)$, $a_{2n}(t)/R_1(t)$, and $b_{2n}(t)/R_2(t)$ for modes n and $2n$, where (a) $n = 9$ and (b) $n = 4$, is depicted in the bottom panels. The physical parameters utilized in (a) are $R_0 = 0.1$, $\beta_{13} = 0.6$, $\beta_{23} = 33\,300$, Ca $= 5000$, and $t_f = 15.95$. In (b), we set $R_0 = 0.2$, $\beta_{13} = 300$, $\beta_{23} = 1000$, Ca $= 5000$, and $t_f = 180.75$.

cases presented in this work, we indeed verify a sizable growth of the amplitudes as time increases, and this destabilization effect is due to the coupling between the interfaces.

Another interesting fact unveiled by Fig. 7(b) is related to the stabilization of the outer leading interface due the presence of the fluid annulus. Even with a high viscosity jump between fluids 2 and 3, the outer interface becomes only modestly disturbed. If one considers the equivalent single-interface problem of a radial displacement of fluid 3 by the injection of fluid 2 in the circumstances of a high viscosity ratio (such as $\beta_{23} = 1000$), the difference in the dynamics is remarkable. As it has been shown by a number of experiments and numerical simulations (see, for instance, Refs. [1–14,22,24–29,39–42]), in the absence of the fluid annulus the displacement is clearly unstable, and the initially circular single interface rapidly deforms, leading to the development of

viscous fingering patterns in which fingers of different lengths compete, spread, and split. This weakly nonlinear theoretical result is consistent with experimental findings of Ref. [16] regarding the role of the fluid annulus in providing an overall attenuation in the growth of instabilities on the outer interface.

The reason for such a stabilizing effect has been provided by the linear analysis performed in Ref. [16]. The authors found that the growth rate of the outer interface has a term that represents a new stabilizing effect which results from the thinning of the intermediate fluid annulus as the interfaces approach one another. A decrease in the magnitude of the intermediate layer tends to stabilize any particular perturbation to the outer interface. Moreover, the stabilization provided by this term is less intense for larger values of viscosity ratio β_{23}. This unique feature is due to the two-interface setup, and there is no analogous term in the single-interface problem.

As a final remark of our work, we would like to mention that the situation in which both interfaces are unstable (i.e., $\eta_1 < \eta_2 < \eta_2$) has also been investigated, but the morphologies obtained for the patterns and the behavior of both interfaces regarding the finger-tip broadening, splitting, and sharpening mechanism were very similar to the ones already explored in Sec. III A.

IV. CONCLUSION

In some practical applications related to extraction of resident fluid out of a porous medium, it's common to pump two or more layers of fluid in sequence into the medium. In such process, the formation of Saffman-Taylor viscous fingering on the interfaces between each layer of fluid can be a issue and potentially reduce the efficiency of this oil recovery strategy. The overwhelming majority of Saffman-Taylor investigations of the radial viscous fingering instability focus on the displacement of two layers of fluid, and only a very few groups have analyzed the problem of the immiscible three-layer radial displacement in a Hele-Shaw cell by performing experiments and employing linear stability analysis.

In this work, we systematically investigated the influence of the fluid annulus on the development of viscous fingering patterns for both the inner and outer interfaces in the injection-driven, three-layer radial Hele-Shaw flow problem. Specifically, we went beyond the linear analysis performed in Refs. [16–21] and made use of an analytical mode-coupling theory to understand how the presence of the fluid annulus impacts the morphology of the weakly nonlinear fingering patterns and also the finger competition mechanism. The main differentiating factor of our model from the purely linear description of the problem is its ability to capture and predict the most prominent nonlinear pattern-forming behaviors via a relatively simple, less expensive theoretical description (in comparison with usual numerical models) of this important but less explored fluid dynamics problem.

By employing a perturbative mode-coupling theory, we have derived a set of coupled equations of motion for each interface. Such nonlinear differential equations describe the time evolution of the perturbation amplitudes of the inner and outer interfaces up to second order in the perturbations (ζ and ε).

First, we analyzed the situation in which the inner interface has an unstable viscosity jump while the outer one is stable. We have found that the initial annulus' thickness d has a great impact on the morphologies of the patterns. For a large value of d (i.e., very thick annulus), we found that the interfaces decouple and disturbances can be seen only on the inner interface. If d is reduced, the coupling between the interfaces becomes stronger and the inner interface induces the development of wide fingers with flat tips on the outer interface. By reducing the value of d even further, we have detected the formation of wide fingers with bifurcated tips and a matching between the final shapes of the interfacial patterns. Surprisingly, for an even thinner annulus, we observed an unexpected change in the morphology of the patterns: broader fingers with bifurcated tips are replaced by narrower sharpened ones. Furthermore, we showed that this changing between finger-widening and -sharpening behaviors are regulated by the initial annulus' thickness and the capillary number. Regarding finger length variability, our findings indicate that smaller values of d lead to an attenuation on finger competition of the outward fingers of both interfaces.

Last, we investigated the opposite case in which the viscosities of the fluids are such that the inner interface is stable and the outer one is unstable. Two main scenarios were revealed: the first one is related to the onset of formation of drops by the rupture of the intermediate layer of fluid, and the second concerns to an overall stabilization of the outer interface by the presence of the fluid annulus. It should be pointed out that these theoretical findings are qualitatively consistent with results obtained in Ref. [16] through experimental investigations performed in similar circumstances.

A possible extension of this work could address fully nonlinear numerical simulations of the immiscible three-layer radial displacement in Hele-Shaw problem. Hopefully, such a numerical study could check some of our weakly nonlinear theoretical findings and also reproduce more accurately the complex formation of drops experimentally revealed in Ref. [16].

ACKNOWLEDGMENTS

S.L. acknowledges the support from the National Science Foundation, Division of Mathematical Sciences grant DMS-1720420. S.L. was also partially supported by grant ECCS-1927432.

APPENDIX: SECOND-ORDER MODE-COUPLING FUNCTIONS

This Appendix presents the expressions for the second-order mode-coupling functions which appear in the text.

In Eq. (12) the second-order terms are given by

$$F(n,n') = \frac{|n|}{R_1}\left\{\frac{1}{2\pi R_1^2}\left[\frac{1}{2} - g_1(n,n')\,\mathrm{sgn}(nn')\right] - \left(\frac{\beta_{13}\beta_{23}}{\beta_{13}-\beta_{23}}\right)\frac{1}{\mathrm{Ca}R_1^3}\left[1 - \frac{n'}{2}(3n'+n)\right]\right\}, \quad \text{(A1)}$$

$$G(n,n') = \frac{1}{R_1}\left\{|n|[1 - g_1(n,n')\,\mathrm{sgn}(nn')] - f_1^{-1}\right\}, \quad \text{(A2)}$$

$$H(n,n') = \frac{|n|}{R_2}\left\{\frac{1}{2\pi R_2^2}\left[\frac{1}{2} - g_2(n')\,\mathrm{sgn}(nn')\right] - \left(\frac{\beta_{23}}{\beta_{23}-1}\right)\frac{1}{\mathrm{Ca}R_2^3}\left[1 - \frac{n'}{2}(3n'+n)\right]\right\}, \quad \text{(A3)}$$

$$I(n,n') = \frac{1}{R_2}\{|n|[1 - g_2(n')\,\mathrm{sgn}(nn')]\}, \quad \text{(A4)}$$

$$J(n,n') = \frac{|n|}{R_1}\left\{\frac{1}{2\pi R_2^2}\,\frac{(A_{23}R^{2|n|}+1)R^{(|n'|-|n|)}}{A_{23}(1-R^{2|n'|})}\,\mathrm{sgn}(nn')\right\}, \quad \text{(A5)}$$

$$K(n,n') = \frac{|n|}{R_1}\left\{\frac{(A_{23}R^{2|n|}+1)R^{(|n'|-|n|)}}{A_{23}(1-R^{2|n'|})}\,\mathrm{sgn}(nn')\right\}, \quad \text{(A6)}$$

$$L(n,n') = \frac{|n|}{R_1}\left\{\frac{1}{2\pi R_1^2}\,\frac{(A_{23}+1)R^{(|n'|+2)}}{A_{23}(1-R^{2|n'|})}\,\mathrm{sgn}(nn')\right\}, \quad \text{(A7)}$$

$$M(n,n') = \frac{|n|}{R_1}\left\{\frac{(A_{23}+1)R^{(|n'|+2)}}{A_{23}(1-R^{2|n'|})}\,\mathrm{sgn}(nn')\right\}, \quad \text{(A8)}$$

where

$$g_1(n,n') = \left(\frac{A_{12}+1}{2A_{12}}\right)\frac{(1+A_{23}R^{2|n|})(1+R^{2|n'|})}{(1-A_{23}R^{2|n|})(1-R^{2|n'|})} + \left(\frac{A_{12}-1}{2A_{12}}\right), \quad \text{(A9)}$$

$$g_2(n') = \frac{A_{23}+1}{A_{23}(1-R^{2|n'|})}, \quad \text{(A10)}$$

and the sgn function equals ± 1 according to the sign of its argument.

The second-order expressions in Eq. (13) are given by

$$\mathcal{F}(n,n') = \frac{|n|}{R_1}\left\{\frac{1}{2\pi R_1^2}\left[\frac{1}{2} - g_3(n')\,\mathrm{sgn}(nn')\right] - \left(\frac{\beta_{13}\beta_{23}}{\beta_{13}-\beta_{23}}\right)\frac{1}{\mathrm{Ca}R_1^3}\left[1 - \frac{n'}{2}(3n'+n)\right]\right\}, \quad \text{(A11)}$$

$$\mathcal{G}(n,n') = \frac{1}{R_1}\{|n|[1 - g_3(n')\,\mathrm{sgn}(nn')]\}, \quad \text{(A12)}$$

$$\mathcal{H}(n,n') = \frac{|n|}{R_2}\left\{\frac{1}{2\pi R_2^2}\left[\frac{1}{2} - g_4(n,n')\,\mathrm{sgn}(nn')\right] - \left(\frac{\beta_{23}}{\beta_{23}-1}\right)\frac{1}{\mathrm{Ca}R_2^3}\left[1 - \frac{n'}{2}(3n'+n)\right]\right\}, \quad \text{(A13)}$$

$$\mathcal{I}(n,n') = \frac{1}{R_2}\left\{|n|[1 - g_4(n,n')\,\mathrm{sgn}(nn')] - f_4^{-1}\right\}, \quad \text{(A14)}$$

$$\mathcal{J}(n,n') = \frac{|n|}{R_2}\left\{\frac{1}{2\pi R_2^2}\,\frac{(A_{12}-1)R^{(|n'|-2)}}{A_{12}(1-R^{2|n'|})}\,\mathrm{sgn}(nn')\right\}, \quad \text{(A15)}$$

$$\mathcal{K}(n,n') = \frac{|n|}{R_2}\left\{\frac{(A_{12}-1)R^{(|n'|-2)}}{A_{12}(1-R^{2|n'|})}\,\mathrm{sgn}(nn')\right\}, \quad \text{(A16)}$$

$$\mathcal{L}(n,n') = \frac{|n|}{R_2}\left\{\frac{1}{2\pi R_1^2}\,\frac{(A_{12}R^{2|n|}-1)R^{(|n'|-|n|)}}{A_{12}(1-R^{2|n'|})}\,\mathrm{sgn}(nn')\right\}, \quad \text{(A17)}$$

$$\mathcal{M}(n,n') = \frac{|n|}{R_2}\left\{\frac{(A_{12}R^{2|n|}-1)R^{(|n'|-|n|)}}{A_{12}(1-R^{2|n'|})}\,\mathrm{sgn}(nn')\right\}, \quad \text{(A18)}$$

where

$$g_3(n') = \frac{A_{12}-1}{A_{12}(1-R^{2|n'|})}, \quad \text{(A19)}$$

and

$$g_4(n,n') = \left(\frac{A_{23}-1}{2A_{23}}\right)\frac{(1-A_{12}R^{2|n|})(1+R^{2|n'|})}{(1+A_{12}R^{2|n|})(1-R^{2|n'|})} + \left(\frac{A_{23}+1}{2A_{23}}\right). \quad \text{(A20)}$$

[1] P. G. Saffman and G. I. Taylor, The penetration of a fluid into a porous medium or Hele-Shaw cell containing a more viscous liquid, Proc. R. Soc. London Ser. A **245**, 312 (1958).

[2] For review papers see, for instance, G. M. Homsy, Viscous fingering in porous media, Annu. Rev. Fluid Mech. **19**, 271 (1987); K. V. McCloud and J. V. Maher, Experimental perturbations to Saffman-Taylor flow, Phys. Rep. **260**, 139 (1995); J. Casademunt, Viscous fingering as a paradigm of interfacial pattern formation: Recent results and new challenges, Chaos **14**, 809 (2004).

[3] J. Bataille, Stabilité d'un écoulement radial non miscible, Rev. Inst. Fr. Pet. Ann. Combust. Liq. **23**, 1349 (1968).

[4] S. D. R. Wilson, A note on the measurement of dynamic contact angles, J. Colloid Interface Sci. **51**, 532 (1975).

[5] L. Paterson, Radial fingering in a Hele-Shaw cell, J. Fluid Mech. **113**, 513 (1981).

[6] S. N. Rauseo, P. D. Barnes, and J. V. Maher, Development of radial fingering patterns, Phys. Rev. A **35**, 1245 (1987).

[7] S. E. May and J. V. Maher, Fractal dimension of radial fingering patterns, Phys. Rev. A **40**, 1723 (1989).

[8] J. D. Chen, Radial viscous fingering patterns in Hele-Shaw cells, Exp. Fluids **5**, 363 (1987).

[9] J. D. Chen, Growth of radial viscous fingers in a Hele-Shaw cell, J. Fluid Mech. **201**, 223 (1989).

[10] H. Thomé, M. Rabaud, V. Hakim, and Y. Couder, The Saffman-Taylor instability: From the linear to the circular geometry, Phys. Fluids **A1**, 224 (1989).

[11] O. Praud and H. L. Swinney, Fractal dimension and unscreened angles measured for radial viscous fingering, Phys. Rev. E **72**, 011406 (2005).

[12] P. Fast and M. J. Shelley, Moore's law and the Saffman-Taylor instability J. Comput. Phys. **212**, 1 (2006).
[13] J. Mathiesen, I. Procaccia, H. L. Swinney, and M. Thrasher, The universality class of diffusion-limited aggregation and viscous fingering, Europhys. Lett. **76**, 256 (2006).
[14] S. W. Li, J. S. Lowengrub, J. Fontana, and P. Palffy-Muhoray, Control of Viscous Fingering Patterns in a Radial Hele-Shaw Cell, Phys. Rev. Lett. **102**, 174501 (2009).
[15] M. Zhao, W. Ying, J. Lowengrub, and S. Li, An efficient adaptive rescaling scheme for computing moving interface problems, Commun. Comput. Phys. **21**, 679 (2017).
[16] S. S. S. Cardoso and A. W. Woods, The formation of drops through viscous instability, J. Fluid Mech. **289**, 351 (1995).
[17] T. H. Beeson-Jones and A. W. Woods, On the selection of viscosity to suppress the Saffman-Taylor instability in a radially spreading annulus, J. Fluid Mech. **782**, 127 (2015).
[18] P. Daripa, Hydrodynamic stability of multi-layer Hele-Shaw flows, J. Stat. Mech.: Theory Exp. (2008) P12005.
[19] P. Daripa, Studies on stability in three-layer Hele-Shaw flows, Phys. Fluids **20**, 112101 (2008).
[20] P. Daripa and X. Ding, Universal stability properties for multi-layer Hele-Shaw flows and application to instability control, SIAM J. Appl. Math. **72**, 1667 (2012).
[21] C. Gin and P. Daripa, Stability results for multi-layer radial Hele-Shaw and porous media flows, Phys. Fluids **27**, 012101 (2015).
[22] J. A. Miranda and M. Widom, Radial fingering in a Hele-Shaw cell: A weakly nonlinear analysis, Physica D **120**, 315 (1998).
[23] J. A. Miranda and M. Widom, Weakly nonlinear investigation of the Saffman-Taylor problem in a rectangular Hele-Shaw cell, Int. J. Mod. Phys. B **12**, 931 (1998).
[24] D. Perugini and G. Poli, Viscous fingering during replenishment of felsic magma chambers by continuous inputs of mafic magmas: Field evidence and fluid-mechanics experiments, Geology **33**, 5 (2005).
[25] I. Bischofberger, R. Ramanchandran, and S. R. Nagel, An island of stability in a sea of fingers: Emergent global features of the viscous-flow instability, Soft Matter **11**, 7428 (2015).
[26] C. Chevalier, M. Ben Amar, D. Bonn, and A. Lindner, Inertial effects on Saffman-Taylor viscous fingering, J. Fluid Mech. **552**, 83 (2006).
[27] G. Bongrand and P. A. Tsai, Manipulation of viscous fingering in a radially tapered cell geometry, Phys. Rev. E **97**, 061101(R) (2018).
[28] D. Pihler-Puzović, P. Illien, M. Heil, and A. Juel, Suppression of Complex Fingerlike Patterns at the Interface Between Air and a Viscous Fluid by Elastic Membranes, Phys. Rev. Lett. **108**, 074502 (2012).
[29] D. Pihler-Puzović, G. G. Peng, J. R. Lister, M. Heil, and A. Juel, Viscous fingering in radial elastic-walled Hele-Shaw cell, J. Fluid Mech. **849**, 163 (2018).
[30] E. Alvarez-Lacalle, E. Pauné, J. Casademunt, and J. Ortín, Systematic weakly nonlinear analysis of radial viscous fingering, Phys. Rev. E **68**, 026308 (2003).
[31] E. Alvarez-Lacalle, J. Ortín, and J. Casademunt, Low viscosity contrast fingering in a rotating Hele-Shaw cell, Phys. Fluids **16**, 908 (2004).
[32] H. Gadêlha and J. A. Miranda, Finger competition dynamics in rotating Hele-Shaw cells, Phys. Rev. E **70**, 066308 (2004).
[33] A. Lindner, D. Derks, and M. J. Shelley, Stretch flow of thin layers of Newtonian liquids: Fingering patterns and lifting forces, Phys. Fluids **17**, 072107 (2005).
[34] J. A. Miranda and E. Alvarez-Lacalle, Viscosity contrast effects on fingering formation in rotating Hele-Shaw flows, Phys. Rev. E **72**, 026306 (2005).
[35] C.-Y. Chen, C.-H. Chen, and J. A. Miranda, Numerical study of pattern formation in miscible rotating Hele-Shaw flows, Phys. Rev. E **73**, 046306 (2006).
[36] R. Folch, E. Alvarez-Lacalle, J. Ortín, and J. Casademunt, Pattern formation and interface pinch-off in rotating Hele-Shaw flows: A phase-field approach, Phys. Rev. E **80**, 056305 (2009).
[37] R. Brandão, J. V. Fontana, and J. A. Miranda, Suppression of viscous fingering in nonflat Hele-Shaw cells, Phys. Rev. E **90**, 053003 (2014).
[38] P. H. A. Anjos and J. A. Miranda, Influence of wetting on fingering patterns in lifting Hele-Shaw flows, Soft Matter **10**, 7459 (2014).

[39] M. J. P. Gingras and Z. Rácz, Noise and the linear stability analysis of viscous fingering, Phys. Rev. A **40**, 5960 (1989).

[40] S. J. Jackson, D. Stevens, H. Power, and D. Giddings, A boundary element method for the solution of finite mobility ratio immiscible displacement in a Hele-Shaw cell, Int. J. Numer. Methods Fluids **78**, 521 (2015).

[41] P. H. A. Anjos, E. O. Dias, and J. A. Miranda, Radial fingering under arbitrary viscosity and density ratios, Phys. Rev. Fluids **2**, 084004 (2017).

[42] P. H. A. Anjos, E. O. Dias, and J. A. Miranda, Fingering instability transition in radially tapered Hele-Shaw cells: Insights at the onset of nonlinear effects, Phys. Rev. Fluids **3**, 124004 (2018).

[43] P. H. A. Anjos, E. O. Dias, and J. A. Miranda, Inertia-induced dendriticlike patterns in lifting Hele-Shaw flows, Phys. Rev. Fluids **2**, 014003 (2017).

[44] J. Nase, D. Derks, and A. Lindner, Dynamic evolution of fingering patterns in a lifted Hele-Shaw cell, Phys. Fluids **23**, 123101 (2011).